Editors' Suggestion

Fermi surface, possible unconventional fermions, and unusually robust resistive critical fields in the chiral-structured superconductor AuBe

Drew J. Rebar,[1] Serena M. Birnbaum,[2] John Singleton,[2] Mojammel Khan,[1,*] J. C. Ball,[1] P. W. Adams,[1] Julia Y. Chan,[3] D. P. Young,[1] Dana A. Browne,[1] and J. F. DiTusa[1]

[1]*Department of Physics and Astronomy, Louisiana State University, Baton Rouge, Louisiana 70803-4001, USA*
[2]*National High Magnetic Field Laboratory, Los Alamos National Laboratory, MS-E536, Los Alamos, New Mexico 87545, USA*
[3]*Department of Chemistry, The University of Texas at Dallas, Richardson, Texas 75080, USA*

(Received 6 December 2018; revised manuscript received 7 February 2019; published 21 March 2019)

The noncentrosymmetric superconductor (NCS) AuBe is investigated using a variety of thermodynamic and resistive probes in magnetic fields of up to 65 T and temperatures down to 0.3 K. Despite the polycrystalline nature of the samples, the observation of a complex series of de Haas–van Alphen (dHvA) oscillations has allowed the calculated band structure for AuBe to be validated. This permits a variety of BCS parameters describing the superconductivity to be estimated, despite the complexity of the measured Fermi surface. In addition, AuBe displays a nonstandard field dependence of the phase of dHvA oscillations associated with a band thought to host unconventional fermions in this chiral lattice. This result demonstrates the power of the dHvA effect to establish the properties of a single band despite the presence of other electronic bands with a larger density of states, even in polycrystalline samples. In common with several other NCSs, we find that the resistive upper critical field exceeds that measured by heat capacity and magnetization by a considerable factor. We suggest that our data exclude mechanisms for such an effect associated with disorder, implying that topologically protected superconducting surface states may be involved.

DOI: 10.1103/PhysRevB.99.094517

I. INTRODUCTION

Noncentrosymmetric superconductors (NCSs) have garnered much attention over the past two decades; their lack of spatial inversion symmetry breaks parity conservation via spin-orbit coupling, possibly resulting in a mixed spin-singlet/spin-triplet superconducting pairing state (see, e.g., Refs. [1–4] and references therein). A spin-triplet state has been reported in both strongly and weakly correlated materials such as $CePt_3Si$ [1] and Li_2Pt_3B [2]. It is possible that the superconducting phases of these materials are topological [5], supporting Majorana fermion surface modes [3]. In addition, it has been predicted that magnetic fields can induce a helical vortex phase in NCSs [4]. Several NCSs have crystal structures that also lack mirror symmetry, so that they are better described as chiral-structured superconductors; these include Li_2Pd_3B [5], Li_2Pt_3B [2], BiPd [6,7], Mo_3Al_2C [8], and preliminarily RhGe [9]. In this context, noncentrosymmetric AuBe is of great potential interest because of its chiral crystal structure along with the presence of the heavy element Au.

AuBe forms in the $B20$ (or FeSi) crystal structure that has attracted attention over the past decade because of the discovery that magnetic materials that have this crystal structure, or that have the $P2_13$ space group, host skyrmion lattice states. Skyrmion lattices are topologically stable field configurations with particlelike properties [10]. Superconductivity in AuBe was originally discovered by Matthias [11], and the material has received more recent interest as a NCS [12,13]. In addition, materials having the $B20$ crystal structure have been predicted to host massless chiral fermions, motivating explorations of their electronic structures [14–16]. A recent report supports this identification in CoSi [17]. Thus, AuBe is an intriguing candidate material to search for unconventional superconductivity associated with its noncentrosymmetric crystal structure in combination with the possible existence of exotic quasiparticles.

In this paper, we extend the previous preliminary explorations to much higher magnetic fields H and lower temperatures T. Our AuBe samples are exceptionally clean, so that, despite their polycrystalline nature, a plethora of de Haas–van Alphen (dHvA) oscillations is observed at moderate-to-high magnetic fields. These dHvA oscillations validate our electronic structure calculations, allowing the Fermi surface of AuBe to be deduced and the density of states at the Fermi energy, vital for an understanding of the superconductivity, to be derived. The application of comprehensive magnetometry, resistivity, and heat capacity experiments at ^{3}He temperatures has expanded the parameter space of the superconducting phase diagram, permitting a type I to type II crossover in the superconducting behavior to be observed. Furthermore, below the crossover, the $T \to 0$ resistive upper critical field is found to exceed that deduced from magnetometry and heat capacity by a factor of around 4, far beyond the expected critical field associated with a common superconducting surface state [18]. This large critical field, plus the observation of nonstandard dHvA oscillations, may be associated with an electronic band in AuBe that is thought to host unconventional fermions.

*Present address: Materials Science Division, Argonne National Laboratory, 9700 South Cass Avenue, Argonne, Illinois 60439, USA.

This paper is organized as follows. Section II covers the sample preparation, experimental techniques, and details of the electronic structure calculations. The normal-state properties, including the dHvA oscillations and their analysis, the calculated Fermi surface, and the heat capacity are described in Sec. III, while Sec. IV gives an account of the superconducting phase diagram. A discussion of our findings and conclusions is given in Sec. V.

II. EXPERIMENTAL AND COMPUTATIONAL DETAILS

Polycrystalline buttons of AuBe were synthesized by arc-melting stoichiometric masses of high-purity elemental Au (shot and wire) and Be (chunks) in an Ar atmosphere. In addition, we found that small single crystals ($0.2 \times 0.05 \times 0.05$ mm^3) formed in a void of a large polycrystalline sample grown via modified Bridgman growth technique employing a beryllium oxide crucible from United Mineral & Chemical Corporation. The polycrystalline samples were characterized by powder x-ray diffraction (XRD) on a Bruker D8 Advance Powder Diffractometer equipped with a LYNXEYE detector.

The polycrystalline samples were cut via electric discharge machining to an elongated bar shape and polished; they were then characterized by heat capacity, dc magnetization, ac magnetic susceptibility, and resistivity measurements. Heat-capacity measurements were performed in a Quantum Design (QD) PPMS system equipped with a ^{3}He insert. Magnetization and ac magnetic susceptibility measurements were carried out in a QD MPMS XL7. The identification of bulk superconductivity in AuBe, as well as the values of the critical fields and temperatures, were verified by magnetization experiments carried out on powdered arc-melted samples and one tiny single crystal [19]. Low-temperature ac magnetic susceptibility was performed within a Janis ^{3}He insert at a frequency of 19 Hz, employing a home-built susceptibility coil set consisting of a primary drive coil and two series counterwound secondary pickup coils. The real part of the ac susceptibility was normalized at 1.8 K to the value reported by the MPMS at 1.8 K. Resistance and magnetoresistance measurements were carried out on rectangular shaped samples with electrical contacts formed via Epotek silver epoxy and thin platinum wires. These measurements employed standard four-probe ac lockin techniques at 19 Hz, both in the MPMS and in the Janis ^{3}He insert.

For the pulsed-field dHvA experiments, polycrystalline needles were inserted into a 0.5-mm bore, 1.5-mm-long compensated-coil susceptometer, constructed from 50-gauge high-purity copper wire. The coil is wound with approximately 610 turns in one sense, followed by around 390 in the opposite sense; final turns are added or subtracted by hand on the bench top to reduce the uncompensated area of the coil to a fraction of a turn [20]. Fine tuning of the compensation is accomplished by electronically adding or subtracting a small part of the voltage induced in a coaxial single-turn coil wound around the susceptometer [20]. Once this has been done, the signal from the susceptometer is $V \propto (\mathrm{d}M/\mathrm{d}t) = (\mathrm{d}M/\mathrm{d}H)(\mathrm{d}H/\mathrm{d}t)$, where M is the magnetization of a sample placed within the bore of the coil and H is the applied magnetic field [20]. Magnetic fields were provided by a 65-T, capacitor-bank-driven pulsed magnet at NHMFL Los Alamos with a rise time to full field of about 10 ms and a downsweep time of about 80 ms (see Fig. 2 of Ref. [21]). The susceptometer was placed within a simple ^{3}He cryostat providing temperatures down to 0.4 K. Magnetic fields were deduced by integrating the voltage (proportional to $\mathrm{d}H/\mathrm{d}t$) induced in an 11-turn coil ($\dot{B}$ coil), calibrated by observing the dHvA oscillations of the belly orbits of the copper coils of the susceptometer [20]. A quantity proportional to the differential susceptibility $\mathrm{d}M/\mathrm{d}H$ can be obtained by dividing the $(\mathrm{d}M/\mathrm{d}t)$ signal by the $\dot{B}$-coil voltage.

Electronic structure calculations were performed using the WIEN2K [22] LAPW density functional software package, using the Perdew-Burke-Ernzerhof [23] generalized gradient approximation (GGA) functional. The experimental lattice constant (see Sec. III A) was used. The Au atom was placed at (u, u, u) with $u = 0.844$, and the Be was positioned at $u = 0.154$. The muffin tin radii used were 2.50 a.u. for Au and 1.90 a.u. for Be. The plane-wave cutoff in the code was varied from R^*K=7.0 to 8.5 to ensure convergence [24], and a 27^3 grid was used for Brillouin zone integrations, which resulted in 654 points in the irreducible zone. Calculations were performed both omitting and including the spin-orbit interaction. This showed that the spin-orbit interaction makes little difference to the overall Fermi-surface topology, but causes an obvious, but small, splitting of the electronic bands except at high-symmetry points of the Brillouin zone. The Fermi surfaces were rendered on a denser grid of 34^3 points. (For clarity, the theoretical Fermi-surface sections shown in Fig. 3 below are plotted for the case of zero spin-orbit interactions.)

III. NORMAL-STATE PROPERTIES

A. Structural details

The room-temperature powder x-ray diffraction measurements confirmed the $B20$ crystal structure (also known as the FeSi structure) [25]. The underlying lattice is simple cubic with four nonequivalent formula units per unit cell, and a lattice constant (unit-cell edge) of 0.4659 nm, in good agreement with earlier work [12,26]. The diffraction measurements also identified small amounts of Au_2Be and BeO in our polycrystalline samples, neither of which is a known superconductor [27,28]. A single crystal [19] was characterized via x-ray diffraction which confirmed the $B20$ crystal structure but identified a high density of twin boundaries.

B. de Haas–van Alphen frequencies

The differential susceptibility $(\mathrm{d}M/\mathrm{d}H)$ measured for both rising and falling magnetic fields using a pulsed-field shot with a maximum field of 40 T is shown in Fig. 1(a). The fact that oscillations in both rising- and falling-field data overlay very well shows that there is little or no inductive heating due to the pulsed magnetic field [29]. Perhaps surprisingly, given the polycrystalline nature of the samples, a plethora of de Haas–van Alphen oscillations of several different frequencies F are observed. The dominant oscillations at low temperature and high fields have $F \approx 2900$–4200 T (see Fig. 2). Figure 1(b) shows that these oscillations persist down to fields of a few Tesla. In addition, the application of a low-pass filter (green curve) reveals that low frequencies $F \approx 100$–200 T

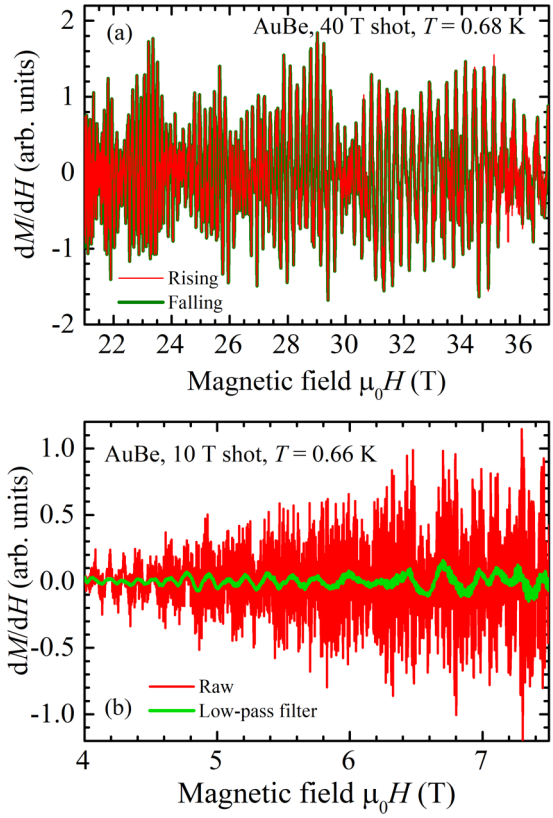

FIG. 1. (a) The differential susceptibility dM/dH plotted versus magnetic field $\mu_0 H$ for a polycrystalline AuBe rod at $T = 0.68$ K, recorded during a 40-T pulsed-magnet shot. Several different series of dHvA oscillations are visible. Data for both rising and falling fields are shown. The "fur" on the data is not noise, but comprises the "belly" orbit dHvA oscillations from the copper of the susceptometer coil. (b) The red trace shows dHvA oscillations recorded using a 10-T pulsed magnet shot ($T = 0.66$ K) where the sample is the same as that used in (a). The green curve represents the application of a low-pass filter to the red trace; this removes the higher-frequency de Haas–van Alphen oscillations so that the lower-frequency series can be seen more readily.

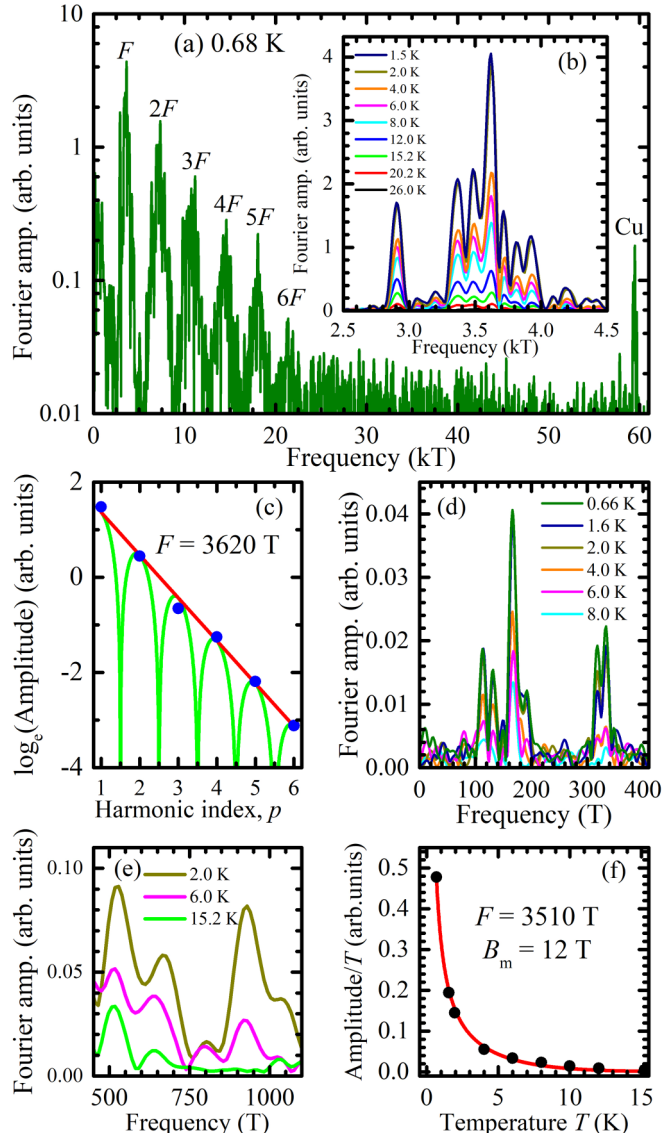

FIG. 2. (a) Fourier spectrum (20–38 T window) of the data in Fig. 1(a) plotted with a logarithmic amplitude scale. A band of several series of dHvA oscillations (labeled F) and their higher harmonics (labeled $2F \ldots 6F$) are clearly visible, along with a peak at 59.5 kT due to the belly orbits in the Cu coil of the susceptometer. (b) Inset: Fourier transforms (linear amplitude scale) of data from 40-T pulses recorded at a series of higher temperatures $T = 1.5$–26 K. The same field window as in (a) has been applied. The frequency range has been chosen to show just the fundamental frequencies in the band of oscillations labeled F in (a). (c) Logarithmic amplitudes (points) of the harmonics of the $F = 3620$ T series of dHvA oscillations versus harmonic index p; the red line is a guide to the eye, showing an approximate linear decrease with p. The green curve is a fit of Eq. (2) for $gm^* = 2$. (d) Fourier transforms of dHvA oscillations from a series of 10-T pulsed-magnet shots at temperatures $T = 0.66$–8.0 K. (e) Field-axis expansion of Fourier transforms (linear amplitude scale) of data from 40-T pulses for three example temperatures, showing frequencies in the range 490–1200 T. The same field window as in (a) has been applied. (f) (Fourier amplitude)/T versus temperature for the $F = 3510$ T series of dHvA oscillations. The data window was centered on $B_m = 12$ T. The red line is a fit of Eq. (4) to the data, yielding $m^* = 0.58 \pm 0.04 m_e$.

are also present, in agreement with measurements of $M(H)$ performed at 1.8 K and fields of up to 7 T in a SQUID magnetometer [13].

The emergence of oscillations with frequencies $F \approx 4000$ T at a field of about 4–5 T [Fig. 1(b)] gives an estimate of the length scale of the disorder encountered by the quasiparticles in the polycrystalline AuBe samples. The cyclotron radius l_c is the characteristic size of the orbitally quantized wave function and is given by

$$l_c = \left(\frac{(2l_{LL} + 1)\hbar}{eB} \right)^{\frac{1}{2}}, \quad (1)$$

where $l_{LL} = F/B$ is the Landau-level index and B is the magnetic flux density [30–32]. Inserting $B = 5$ T and $F = 4000$ T yields $l_c \approx 0.46$ μm. Optical microscopy of our polycrystalline AuBe samples indicates grain sizes spanning the range ~1–50 μm. Therefore, one possible explanation for the low-field onset of the dHvA oscillations in Fig. 1(b) is that when the magnetic field exceeds ≈4–5 T, the cyclotron radius

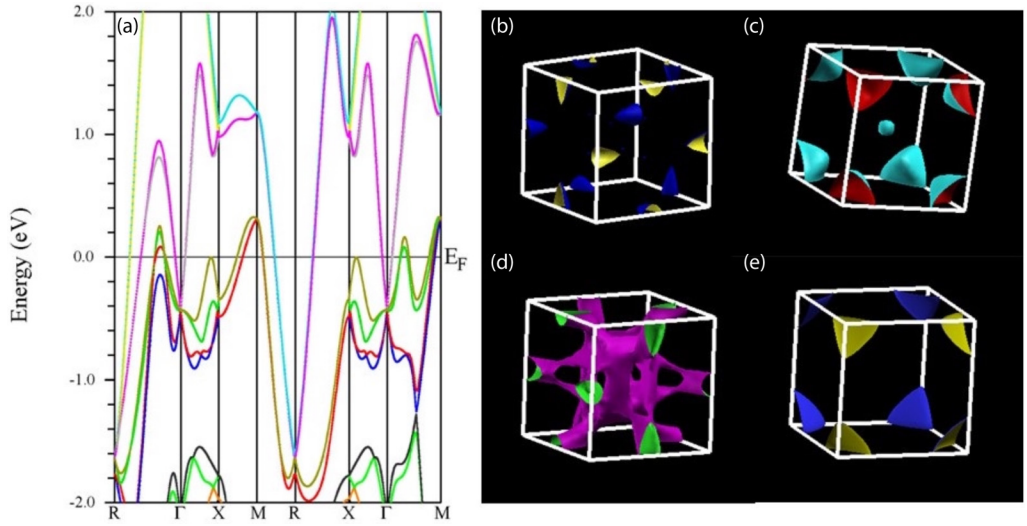

FIG. 3. (a) Calculated electronic structure of AuBe including spin-orbit coupling and (b)–(e) the predicted Fermi-surface sections shown within the simple-cubic Brillouin zone. For clarity, the predicted Fermi pockets are shown here without the slight doubling of surfaces due to band splitting caused by the spin-orbit coupling. (b) Hole ellipsoids centered on the zone-edge M points. (c) An electron approximate superellipsoid centered on the zone-corner R point, plus a small, approximately spherical, electronlike pocket at the zone-center Γ point; (d) a "monster" [31] spanning most of the Brillouin zone; and (e) a second, electron approximate superellipsoid centered on the zone-corner R point. As is conventional, the terms "electron" and "hole" are used for Fermi-surface sections for which the effective masses are, respectively, positive and negative [31].

becomes small enough for the Landau wave functions to fit comfortably within even the smallest grains, so that dHvA oscillations emerge and their amplitudes begin to follow the Lifshitz-Kosevich formula [31] with a constant scattering rate determined by impurities within the grains [32]. As the field is lowered below ≈4–5 T, the cyclotron radius grows to the typical size of the grains and increasing numbers of quasiparticles encounter the boundaries, causing the scattering rate to increase and the oscillations to vanish.

Figures 2(a) and 2(b) show the Fourier spectra (20–38 T window) of the data in Fig. 1(a) and similar pulses recorded at higher temperatures. As mentioned above, the spectra are dominated by several series of dHvA oscillations with frequencies spanning the range $F \approx 2900$–4200 T [Fig. 2(b)], plus their harmonics $2F, 3F \ldots 6F$ [Fig. 2(a)]. The presence of the higher harmonics is suggestive of exceptionally sharply defined Landau levels, due to low quasiparticle scattering rates [31].

For fixed magnetic field and temperature, the Lifshitz-Kosevich formula [31] predicts that the amplitude A of a series of de Haas–van Alphen oscillations should depend on harmonic index p as follows:

$$A \propto R_{\mathrm{D}} \cos\left(\frac{p\pi g m^*}{2}\right) = e^{-\frac{\pi p}{\omega_{\mathrm{c}}\tau}} \cos\left(\frac{p\pi g m^*}{2}\right), \qquad (2)$$

where R_{D} is often known as the *Dingle factor*. Here, $\omega_{\mathrm{c}} = \frac{eB}{m^*}$ is the cyclotron frequency, τ is the scattering time, B is the magnetic flux density [30], g is the g factor, and m^* is the quasiparticle effective mass. In order to estimate τ from the harmonic series, we choose a particular series of dHvA oscillations (fundamental frequency $F = 3620$ T) with a logarithmic amplitude that falls off roughly linearly with p [see Fig. 2(c)]. Such a linear relationship implies that $gm^* \approx 2$ (or $2n$, where n is a nonzero integer), so that the phase of the cosine term in Eq. (2) is approximately constant at each value of p. Using the effective mass $m^* = 0.67 m_{\mathrm{e}}$ (see following section), a fit of the Fourier amplitudes to Eq. (2) for harmonics $p = 1$–6 [Fig. 2(c)] yields $\tau = 0.5 \pm 0.1$ ps, comparable to the scattering times observed in, e.g., high-purity copper [31]. Such values are supported by the large residual resistivity ratio (RRR) values of the AuBe samples, discussed in Sec. IV B. The value $g \approx 3$ implied by $gm^* \approx 2$ is not unusual for metals with moderate spin-orbit interactions and electron-electron interactions [31].

The lower-frequency dHvA oscillations are revealed more clearly by Fourier transforms with a lower-field window [4–9 T; see Fig. 2(d)] [33]. Here, several frequencies in the range 100–200 T are observed, with a dominant peak around 170 T, representing an orbit area that is about 0.90% of the square cross-sectional area of the Brillouin zone. There are two further peaks between 300 and 350 T, the higher of which is almost certainly a second harmonic of the 170-T frequency.

Figure 3 shows the calculated band structure and Fermi-surface sections for AuBe inside the simple-cubic Brillouin zone. The band structure shown in Fig. 3(a) is similar to that published previously [12] and has many features in common with the band structure of other $B20$ materials [14–16,34]. This includes what has previously been described as a fourfold-degenerate chiral fermion ∼0.4 eV below the Fermi energy at the Γ point and a chiral double sixfold-degenerate spin-1 Weyl node nearly 2 eV below the Fermi level at the R point of the Brillouin zone [15,16].

The Fermi surface comprises hole ellipsoids centered on the zone-edge M points [Fig. 3(b)], two electron approximate superellipsoids centered on the zone-corner R points [Figs. 3(c) and 3(e)], a small, approximately spherical electron pocket at the zone-center Γ point [Fig. 3(c)] and what

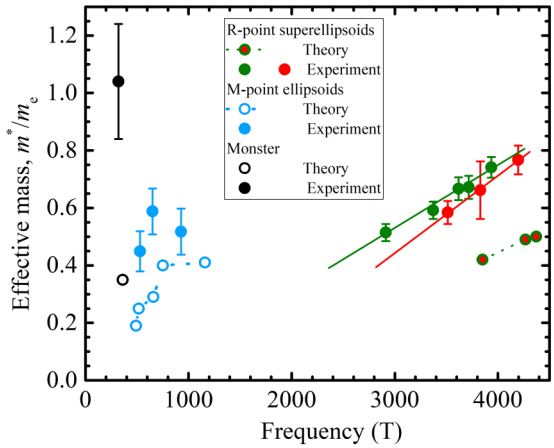

FIG. 4. Solid points represent effective masses derived using Eq. (4) versus corresponding experimental dHvA frequencies. The error bars are the uncertainties given by the simplex fitting routine and the different colored points and guidelines are explained in the text. Masses and frequencies corresponding to a selection of predicted extremal orbits from the band structure calculations (including spin-orbit interactions) are shown as hollow points. The hollow light-blue points (calculated for $\mathbf{H} \parallel [100]$; dotted line is a guide to the eye) correspond to the hole ellipsoids centered on the zone-edge M points [Fig. 3(b)]. The hollow green, red-filled points (calculated for $\mathbf{H} \parallel [100]$) are from the two electron approximate superellipsoids centered on the zone-corner R points [Figs. 3(c) and 3(e)]. The black, hollow point corresponds to a possible "monster" extremal orbit [Fig. 3(d)].

old-school fermiologists would call a *monster* [31] of holes [Fig. 3(d)].

For a polycrystalline sample, the dHvA signal will be dominated by Fermi-surface pockets that possess either several extremal orbits that are identical or similar in cross-sectional area, or a region in which the extremal orbit area varies slowly with magnetic field orientation [31]. The predicted Fermi surface contains several candidate pockets that might cause the observed dHvA oscillations. For example, the R-point pockets sport extremal cross-sectional areas encompassing the spread of frequencies shown in Fig. 2(b). The largest and smallest calculated extremal orbits about the M-point ellipsoids are equivalent to frequencies of 491 and 1160 T, a range that again encompasses observed peaks in the Fourier transforms [Fig. 2(e)]. The small Γ-point pocket is predicted to have cross sections corresponding to $F = 230$–271 T, somewhat larger than the pocket suggested by the dominant low-frequency oscillation with $F = 170$ T. We will return to a more detailed summary of these attributions in the discussion of Fig. 4.

C. Quasiparticle effective masses

In allocating the various series of dHvA oscillations to the predicted Fermi-surface sections, it is useful to examine the relationship of their effective masses to their frequencies. The effective mass m^* given by a dHvA experiment is defined by [31,35]

$$m^* = \frac{\hbar^2}{2\pi}\frac{\partial S}{\partial E}, \tag{3}$$

where S is the k-space cross-sectional area of the extremal orbit in the plane perpendicular to the magnetic field and E is the quasiparticle energy. Through the Onsager relationship $F = \frac{\hbar}{2\pi e}S$, the dHvA frequency F is directly proportional to S [31]. Therefore, if several series of dHvA oscillations, corresponding to different orientations of the magnetic field with respect to the crystal axes, are derived from one particular band, and this band has a dispersion relationship $E(\mathbf{k})$ close to the Fermi energy E_F, then a plot of m^* versus F will lie on a curve that is characteristic of $E(\mathbf{k})$. As a simple example, suppose that the dispersion relationship close to E_F is described by $E \propto k^r$, where r is a constant, then $F \propto S \propto E^{\frac{2}{r}}$ and $m^* \propto E^{\frac{2}{r}-1}$. Thus, a plot of m^* versus F will have a form determined by the dispersion relationship (see Ref. [36] and references therein).

Figure 2 shows that dHvA effect is observable over a wide range of temperature T, so that the Fourier amplitudes $A(T, B_m)$ can be fitted to the temperature-dependent part of the Lifshitz-Kosevich formula [31]

$$\frac{A(T, B_m)}{T} \propto \frac{(14.69m^*/B_m)}{\sinh(14.69m^*T/B_m)}, \tag{4}$$

where B_m is the inverse-field midpoint of the field window used for the Fourier transform:

$$B_m = \left[\frac{1}{2}\left(\frac{1}{B_l} + \frac{1}{B_u}\right)\right]^{-1}. \tag{5}$$

Here, B_l and B_u are, respectively, the lower and upper field limits of the window.

Amplitudes from the various series of dHvA oscillations were fitted numerically to Eq. (4) [Fig. 2(f)]. The $F \approx 170$ T series of dHvA oscillations exhibits a field-dependent effective mass and will be discussed in more detail below. The other dHvA frequencies behave in a more conventional manner, yielding masses that are field independent within experimental precision.

Experimental effective masses are plotted against their corresponding dHvA frequencies in Fig. 4 as solid points. The predicted extremal orbits and the magnitudes of the cyclotron effective masses from the band structure calculations (including spin-orbit interactions) are shown as hollow points on the same diagram. The cluster of frequencies (solid green and red points in Fig. 4) spanning the range $F = 2900$–4200 T [Figs. 2(a) and 2(b)] possess masses from $0.4m_e$ to $0.8m_e$, with m^* approximately proportional to F. It is possible that these masses in fact lie on two separate curves (indicated by the red and green lines in Fig. 4). This suggests that all of these dHvA frequencies are derived from one or, if one believes the separate green and red curves, two bands of similar E versus k curvature. The theoretical m^*, F values (green, red-filled, hollow points; calculated for $\mathbf{H} \parallel [100]$) for the two electron approximate superellipsoids centered on the zone-corner R points [Figs. 3(c) and 3(e)] vary in a similar way to the cluster of experimental points, albeit with lower effective masses. These Fermi-surface sections are therefore very likely to be responsible for the band of dHvA frequencies from $F = 2900$–4200 T seen in experiments.

The solid light-blue (experimental) points in Fig. 4 group around a mass of $0.5\,m_e$ and possess frequencies spanning 530–930 T [Fig. 2(e)]. The predicted m^*, F values (hollow

light-blue points; calculated for $\mathbf{H} \parallel [100]$) for extremal orbits of the hole ellipsoids centered on the zone-edge M points [Fig. 3(b)] follow a very similar pattern; it is therefore likely that these Fermi-surface pockets are responsible for the experimental dHvA frequencies shown as light-blue points. As in the case of the R-point Fermi-surface sections the calculation underestimates the m^* values.

The solid black point in Fig. 4 possesses a low-frequency ($F = 320$ T) but a substantially higher mass compared to the other oscillation series observed in the experiments. It is possible that this frequency corresponds to one of the cross sections of the "monster" [Fig. 3(d)]. The band structure calculations yield several extremal orbits about the monster, both electronlike and holelike, with dHvA frequencies F ranging from 181 to 790 T and effective mass magnitudes from 0.18 to $0.77m_e$. One of these (black, hollow point) has $F = 361$ T, and is a promising candidate, possessing an extremal orbit area that varies relatively slowly with angle. Just as in the other instances, the effective mass is underestimated by the calculation, in this case substantially.

The behavior of the $F \approx 170$ T series of dHvA oscillations is more unusual. As noted above, this frequency likely results from the approximately spherical pocket at the zone-center Γ point [Fig. 3(c)]. Our band structure calculations suggest that this band possesses a linear E versus k (Dirac-type) dispersion relationship, with the Dirac point [37] some 400 meV below the Fermi energy. The corresponding dHvA oscillations possess a phase that is difficult to track as a function of field, plus an effective mass that is field dependent. In order to investigate these effects, Fourier transforms of $\mathrm{d}M/\mathrm{d}H$ data are taken with lower and upper limits given by

$$B_\mathrm{l} = \left(\frac{1}{B_\mathrm{m}} + \frac{\Delta}{2}\right)^{-1} \quad \text{and} \quad B_\mathrm{u} = \left(\frac{1}{B_\mathrm{m}} - \frac{\Delta}{2}\right)^{-1}, \qquad (6)$$

where the inverse field window Δ was kept constant at $1/24$ T^{-1} and the center field B_m was varied in steps of 0.25 or 0.5 T. As well as the amplitude and frequency of each oscillation series, the Fourier-transform routine produces the phase $\aleph$ of each oscillation series, defined as

$$\left(\frac{\mathrm{d}M}{\mathrm{d}H}\right)_{\mathrm{osc},F} \propto \cos\left(2\pi\frac{F}{B} + \aleph\right), \qquad (7)$$

where the subscript "osc, F" indicates the oscillatory component of the susceptibility associated with the dHvA oscillations of frequency F. The Fourier amplitudes from different temperature data can be used to derive the effective mass for each value of the center field [see Eq. (4)]. To ensure that the mass values were not overestimates, only data for temperatures at which the Fourier amplitude was well above the noise floor were used in these fits [38].

To exclude the possibility that the effects under discussion are due to a superposition of several dHvA frequencies close to 170 T with different masses and scattering times, several precautions were taken. (i) The field window used for the Fourier transforms was wide enough so that any movement, growth, or change in shape/width of the Fourier peaks due to the emergence of another dHvA series would be well resolved. Thus, the appearance of a slightly different dHvA frequency as the field or temperature changed would be noticeable as an alteration in the width or shape of the peak under study. Careful observations were made to ensure that this did not occur, e.g., as the frequency of the 170-T series shifted as the Fourier window moved to higher fields, checks were made to see that there was no peak left behind at the original frequency. (ii) The presence of similar frequencies with different masses and phases would tend to lead to a shift in frequency and/or phase as the heavier-mass series died away with increasing temperature, leaving the lighter-mass oscillations behind. This was excluded by ensuring that the detected frequency and phase of the 170-T series remained the same for a particular field window as the temperature varied. (iii) Finally, high-field (65-T) shots and varying Fourier window widths were used to see whether multiple peaks emerged around 170 T; this did not occur, suggesting that the 170-T series is alone.

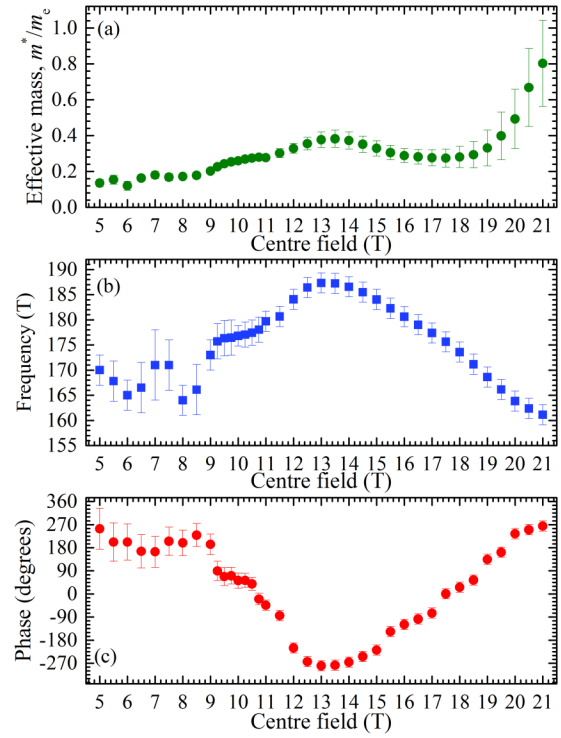

FIG. 5. Magnetic field dependence of parameters describing the $F \approx 170$ T series of dHvA oscillations: (a) effective mass m^*, (b) frequency F, and (c) phase $\aleph$ [see Eq. (7)] of the oscillations. The field dependencies of these parameters are derived from Fourier analysis of $\mathrm{d}M/\mathrm{d}H$ data using inverse field windows of $\frac{1}{24}$ T^{-1} width symmetrically disposed (in inverse field) about the center field (B_m) values given on the lower axis.

The results of the above procedure are plotted in Fig. 5. As can be seen, the effective mass, frequency, and phase of the $F \approx 170$ T dHvA oscillations all vary with magnetic field, with the mass showing a gradual, but quite spectacular (factor 5) increase. Possible causes for such an effect include a field-induced change in the energy of the corresponding band relative to the Fermi energy, a field-induced change in its curvature, a field-induced alteration of the many-body effects contributing to the quasiparticle effective mass, or a combination of all three. All of these possible effects would alter the distribution of quasiparticles between this band and

the reservoir provided by the other Fermi-surface pockets, resulting in changes to either or *both* the dHvA frequency and the phase of the oscillations [39]. However, the changes that we measure to the frequency, effective mass, and phase of the $F \approx 170$ T dHvA oscillations are starkly atypical. We are aware of only a small number of materials that exhibit a subset of these features, such as a field-induced change (increase or decrease) in effective mass in metallic systems associated with Kondo-type phenomena [20,41], a class of materials that does not include AuBe. However, we point out that the Dirac-type band [Fig. 3(a)] that we have associated with this series of dHvA oscillations has been predicted, in this class of materials, to undergo a drastic change with the application of magnetic field [15]. Here, the quasiparticles associated with this band are expected to split into multiple Weyl fermions due to a breaking of time-reversal symmetry. This unusual modification would have a dramatic effect on the dHvA oscillation frequency and phase, as well as the effective mass. Our data suggest that the characteristic field for the changes to be experimentally observable is approximately 9 T. Below this field, the oscillations in dM/dH have a roughly constant phase, similar to that expected for the Fermi surface of a conventional metal [31]. Above 9 T, the phase starts to vary, in places exceeding the extra π Berry phase associated with a single species of Weyl fermion [15]. (This shift in phase of the oscillations with field is the probable reason for an earlier lack of success in determining an unambiguous Berry phase associated with the Dirac-type dispersion relationship [13].)

D. Heat capacity

The low-temperature heat capacity C of AuBe is displayed in the form C/T versus T^2 in Fig. 6(a). Here, the superconducting transition is visible as a jump close to $T^2 = 10$ K^2 in the $H = 0$ data set. The normal state is restored by fields of a few tens of mT (see Sec. IV), yielding the expected linear relationship [42]

$$\frac{C}{T} = \gamma + \beta T^2, \tag{8}$$

where γ and β represent electronic and phonon contributions, respectively. Straight-line fits of the $H = 0$ data set for temperatures above the superconducting transition and to the $\mu_0 H = 50$ and 300 mT data yield $\gamma = 1.85 \pm 0.06$ mJ mol^{-1} K^{-2} and $\beta = (1.51 \pm 0.05) \times 10^{-4}$ J mol^{-1} K^{-4}. The value of γ is in good agreement with previous studies [12,13]. Using our calculated electronic density of states at the Fermi energy, $g(E_F) \approx 0.59$ states eV^{-1}(formula unit)$^{-1}$ and the equation [42]

$$\gamma = \frac{\pi^2}{3} k_B^2 g(E_F), \tag{9}$$

we obtain a theoretical value $\gamma = 1.39$ mJ mol^{-1} K^{-2}, around 25% lower than the experimental value. In a similar way, the band structure calculation underestimates the effective masses compared to those determined from the temperature dependence of the dHvA oscillations (see Fig. 4). This suggests that many-body effects not included in our calculation contribute to the $g(E_F)$ and m^* values observed experimentally [35,42].

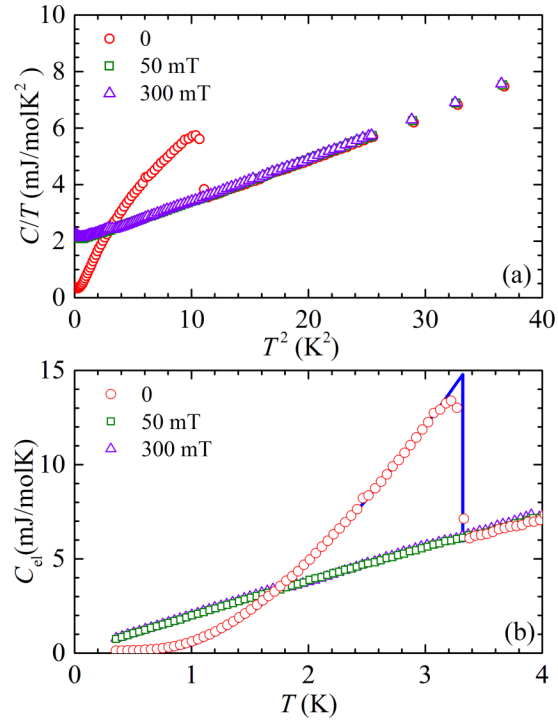

FIG. 6. (a) Heat capacity C of AuBe, divided by temperature T, plotted as a function of T^2 at fields $\mu_0 H = 0$, 50, and 300 mT. The transition to the superconducting state is marked by the near-vertical jump close to $T^2 = 10$ K^2 in the $H = 0$ data set. (b) The low-temperature electronic component of the heat capacity versus T at fields of $\mu_0 H = 0$, 50, and 300 mT. The curve is a fit to the standard BCS model for an isotropic, fully gapped superconductor in the weak-coupling limit [44].

The low-temperature phonon contribution C_{phonon} to the heat capacity is

$$C_{phonon} = \frac{12\pi^4 N k_B}{5}\left(\frac{T}{\theta_D}\right)^3 \equiv \beta T^3, \tag{10}$$

where θ_D is the Debye temperature [42] and N is the number of atoms per formula mole. For AuBe, $N = 2N_A$, where N_A is Avogadro's number. Hence, the above value of β can be used to derive $\theta_D = 295 \pm 3$ K for AuBe [43].

IV. SUPERCONDUCTING STATE

A. Heat-capacity discontinuity

Figure 6(b) shows the electronic heat capacity C_{el} obtained by subtracting the phonon contribution βT^3 from C, using the value of β determined above. The superconducting transition in zero applied field is observed at $T_c = 3.3 \pm 0.1$ K, with no indication of superconductivity in fields $\mu_0 H \geqslant 50$ mT. The BCS form of the electronic heat capacity from the work of Mühlschlegel [44] fitted the data below the superconducting transition very well. The ratio of the jump in heat capacity ΔC at T_c and the normal-state electronic heat capacity C_n above the transition was calculated to be $\Delta C/C_n = 1.48$, a value close to the expected BCS value of 1.43. Thus, the heat capacity of AuBe is well described by the standard model

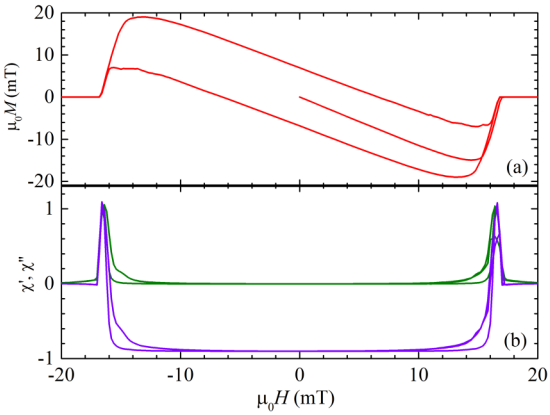

FIG. 7. (a) The dc magnetization M (red) versus field H at a temperature of $T = 1.8$ K. Sharp transitions and a small supercooling, evident in the hysteresis of the critical field, are apparent in $M(H)$. (b) The real component χ' (purple) and the imaginary component χ'' (green) of the ac magnetic susceptibility versus H, again at $T = 1.8$ K.

for an isotropic, fully gapped superconductor in the weak-coupling limit [44].

B. Field-temperature phase boundary

Figure 7 shows the dc magnetization and ac magnetic susceptibility as a function of magnetic field at $T = 1.8$ K, where the field has been taken through a complete 0 to 40 to −40 to 40 mT field cycle. The dc magnetization is that of a type I superconductor with sharp transitions at the critical field H_c, a small level of supercooling evident in the hysteresis of the critical field [45], and a slope in the superconducting state of $(dM/dH) = -1.1$. This slope is compatible with a demagnetization factor of $N \approx 0.2$ for the bar-shaped sample [aspect ratio = length/(square cross-sectional side) ≈ 2] [46] and suggests a Meissner effect of −0.90, a figure close to the expectations [42,45] for a full Meissner effect of $\chi = -1$. Additionally, measurements on an indium sample of similar dimensions resulted in a nearly identical Meissner effect, confirming the deduced value of χ.

The ac magnetic susceptibility in Fig. 7(b) has been corrected for demagnetizing effects. The real component of the ac susceptibility (χ') displays a sharp peak at approximately the midpoint of the superconducting transition. This peak, known as the differential paramagnetic effect (DPE), occurs in the intermediate state $[(1-N)H_c \leqslant H \leqslant H_c]$ and indicates a sudden expulsion or inclusion of magnetic flux consistent with type I [47] or, rarely, soft type II superconductivity [18,48]. Therefore, the superconducting behavior of AuBe near T_c indicates a typical type I response to applied field [18,45,48,49].

Figures 8(a) and 8(b) display the temperature dependence of the ac magnetic susceptibility down to 0.3 K. An interesting feature of these data is the suppression, and eventual disappearance, of the DPE peak in the real component χ' as the sample is cooled below 1.2 K. This is accompanied by a significant increase in the width of the superconducting transition (in both χ' and χ'') below 1.2 K. The loss of the

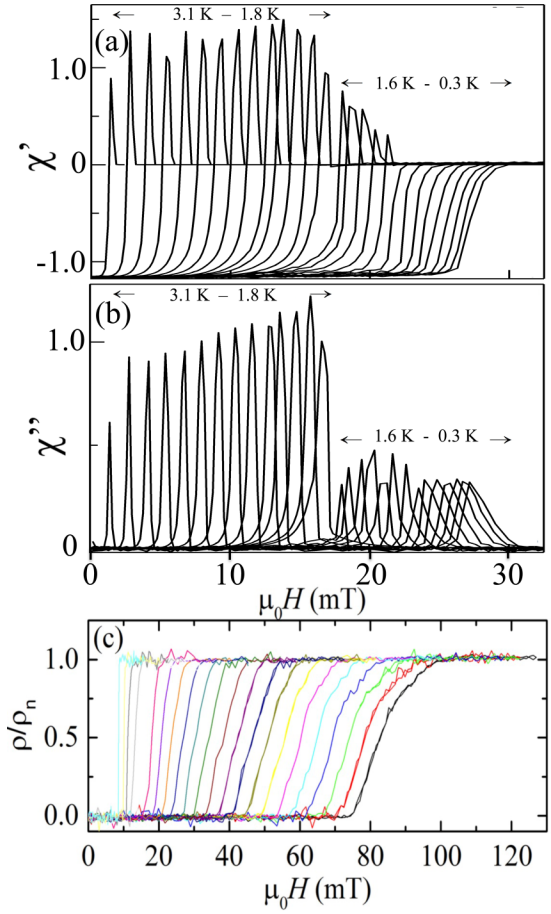

FIG. 8. Real component χ' (a) and imaginary component χ'' (b) of the magnetic susceptibility of a polycrystalline bar of AuBe plotted against H for a series of constant temperatures in the range $3.1\ \text{K} \geqslant T \geqslant 0.3$ K. Field sweeps in the temperature range 0.3–1.6 K were done in the ^{3}He cryostat, while those in the range 1.8–3.1 K employed the MPMS. The jump in peak magnitudes between 1.6 and 1.8 K is caused by a difference in drive amplitude. (c) Isothermal resistivity data, shown as resistivity ρ divided by the low-temperature normal-state resistivity ρ_n versus magnetic field H. The data were recorded at a series of approximately equally spaced temperatures covering the range $3.0\ \text{K} \geqslant T \geqslant 0.3$ K.

DPE peak and widening of the transition to the normal state suggest a crossover into the type II superconducting regime [50]. Therefore, at low temperatures, AuBe seems to be a type II superconductor with a Ginzburg-Landau parameter $\kappa = \lambda/\xi$, where λ is the London penetration depth and ξ is the coherence length, not much larger than $1/\sqrt{2}$, so that warming above 1.2 K leads to a transition to type I behavior [45,50]. Similar behavior in disordered elemental superconductors was investigated thoroughly decades ago and was termed *type 1.5* or *type II/1 superconductivity* [45,51,52] ($\kappa \approx 1/\sqrt{2}$), though it should be noted that the former term has more recently taken on a new meaning [53]. Recently, a similar suppression of the DPE in $PdTe_2$ with cooling below 1.5 K was attributed to screening via a superconducting surface layer [47]. We cannot rule out such a mechanism for AuBe.

The resistivity of AuBe was measured from 0.3 K to room temperature with a focus on the transition between the

normal and superconducting states. Although our samples are polycrystalline, having been synthesized via arc melting, and despite the presence of a small density of other phases, we find resistivities ρ as low as 0.2 $\mu\Omega$ cm at 4 K and a residual resistivity ratio RRR $= \rho(300\ \mathrm{K})/\rho(4\ \mathrm{K}) = 80$, commensurate with the large-amplitude dHvA oscillations discussed in earlier sections. Figure 8(c) displays the resistivity ρ divided by the low-temperature normal-state resistivity ρ_n as a function of applied field for $T < T_c$. While superconducting transitions are consistent with critical values and widths determined from the magnetic characterization for $T > 2.4$ K [compare Figs. 8(a) and 8(b)], the critical fields for $T < 2.4$ K are significantly higher than those deduced from $M(H)$, or expected for a surface state from Ginzburg-Landau theory [45,50] ($H_{c3} \approx 1.7H_{c2}$). In agreement with the broadening of the transition widths found in $\chi(H)$ below 1.2 K in Figs. 8(a) and 8(b), the resistivity transitions broaden in a similar fashion at the proposed crossover from type I to type II superconductivity.

To further elucidate the nature of the enhanced critical field in ρ and compare the behavior of AuBe at fields above H_{c2} to that of a more standard type II superconductor hosting a superconducting surface sheath, a Cr film of thickness between 5 and 10 nm was deposited on the surface of two AuBe samples. In this way, a pair-breaking magnetic material [50] has been introduced on all surfaces of the samples. Both trials saw no reduction in the critical fields as determined from $\rho(H)$ measurements. Thus, resistivity measurement and subsequent Cr depositions revealed enhanced field critical values at low temperatures that result from either a surface state that is insensitive to magnetic scattering or, perhaps, a filamentary superconductivity in the bulk of AuBe.

Figure 9(a) displays the superconducting phase diagram for the critical temperatures T_c and critical fields H_c determined from what might be termed bulk thermodynamic probes (heat capacity, magnetization, susceptibility), and resistivity measurements. The critical fields and temperatures are defined by the discernible onset of superconductivity in the particular measurement technique. [We also include critical fields determined from measurements of the magnetization of a small single crystal for comparison to the polycrystalline results. Apart from a very slight increase in T_c, these data reproduce the data determined from the polycrystalline samples in the temperature range explored ($T > 1.7$ K).] The main result is abundantly clear; the critical field determined from $\rho(H, T)$, $H_{c\rho}$, diverges from that determined from $M(H)$ and χ' at approximately 2.4 K, rising almost linearly to an extrapolated $T = 0$ intercept of approximately 130 mT. The magnetization critical fields follow a less unusual variation, yielding $T_c(H = 0) = 3.25$ K and $H_c(T = 0) = 31 \pm 1$ mT. Superconducting fluctuations are not the cause for this large enhancement of the resistive critical field since the critical field determined from the highest field displaying zero resistance, shown in Fig. 9(a), extrapolates to approximately 84 mT at $T = 0$. This critical field is over 2.6 times larger than $H_c(T = 0)$.

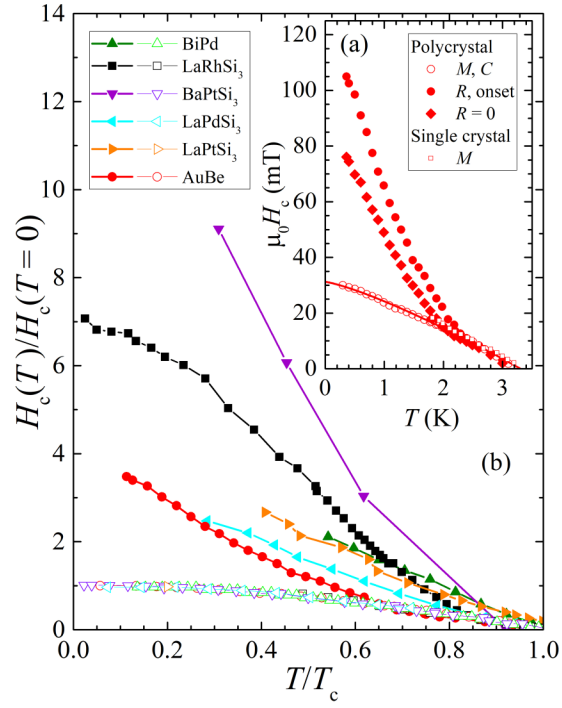

FIG. 9. (a) Inset: critical fields versus temperature for AuBe. The solid symbols are critical fields measured using resistivity (circles = onset of resistive transition, diamonds = highest field at which zero resistance occurs), while the hollow symbols represent critical fields derived from thermodynamic probes (magnetization, susceptibility and heat capacity). Data from the magnetization of a small single crystal are shown as hollow squares. (b) Analogous phase diagram for a representative collection of NCSs, presented in reduced units $H_c/H_c(T = 0)$, T/T_c. Here, $H_c(T = 0)$ is derived from standard BCS fits to critical fields derived from thermodynamic probes. As in (a), open symbols represent thermodynamic critical fields and filled points are resistive critical fields. Data for the various NCSs are from the following sources: AuBe (this work), BiPd [60], $LaRhSi_3$ [61], $BaPtSi_3$ [62], $LaPdSi_3$ [56], $LaPtSi_3$ [56].

V. DISCUSSION

The investigation presented here has permitted a fuller impression of the normal and superconducting properties of AuBe, including its electronic structure. To place AuBe in context with conventional superconductors and other NCSs, we have used these experimental data to make estimates of the most usual parameters used to describe the superconducting state. In common with many of the weakly correlated NCSs [54,55] and in agreement with Ref. [12], the fact that the heat capacity of AuBe can be well described by the standard BCS form for an isotropic superconducting gap with singlet pairing [Fig. 6(b)] places limits on the size of the possible triplet contributions to the superconducting wave function. Therefore, we use the BCS expression [45] $\Delta = 1.764 k_B T_c(H = 0)$ to derive $\Delta = 0.49$ meV. Furthermore, using the measured dHvA frequencies (i.e., Fermi-surface cross-sectional areas) and effective masses, an average Fermi velocity $v_F \approx 3.8 \times 10^5$ ms^{-1} can be estimated. Inserting this into the BCS expression [45,50] $\xi = \frac{\hbar v_F}{\pi \Delta}$, a coherence length of $\xi \approx 160$ nm results. Similarly, the calculated band structure yields an averaged effective mass m^* and effective quasiparticle density n that can be used to estimate the penetration depth [45,50] $\lambda = \sqrt{\frac{m^*}{\mu_0 n q^2}} \approx 120$ nm, where q is the electronic charge. Therefore, the Ginzburg-Landau parameter $\kappa = \lambda/\xi \approx 0.75$, rather consistent with the expectations for type II/1

superconductivity [45,51,52] ($\kappa \approx 1/\sqrt{2} \approx 0.71$) discussed in Sec. IV. A second value of κ can be derived from a fit of the BCS parabolic form of the critical field to the type II region of the phase diagram [45,50]. This gives $\mu_0 H_{c2} = 31$ mT, yielding $\kappa = H_{c2}/(\sqrt{2}H_c) \approx 0.87$, reasonably close to the value of 0.75 derived from the estimated ξ and λ, giving us confidence in our estimates.

The crossover from type II (low T) to type I (higher T) superconductivity in AuBe is similar to behavior that was investigated decades ago in elemental superconductors that were intentionally disordered [51,52]. Although type I superconductivity is usually associated with pure elements, and type II with compounds, a trend is apparent in that several NCSs display type I behavior [56–59]. Since carrier scattering limits the superconducting coherence length, type I behavior in AuBe is likely connected to the long mean-free path of charge carriers evident in the very small resistivity found at low temperature, the observation of dHvA oscillations at fields as small as 2 T, and the long scattering time derived from the sequence of harmonics in the dHvA oscillations. The picture of AuBe that emerges is that of a low-scattering-rate NCS that resides near the border between type I and II superconductivity.

Perhaps the most interesting aspect of the superconductivity of AuBe is the enhancement of $H_{c\rho}$ beyond the critical field H_{c3} that would be expected for a superconducting surface state [45]. This enhancement is unlikely to be due to defects or to impurity phases residing at surfaces or interfaces of our samples. This follows from several important observations including the correspondence of the critical fields presented in Fig. 9 for $T > 2.4$ K where type I behavior is apparent. A superconducting surface state is not expected in materials well into the type I regime [45] ($\kappa < 1/\sqrt{2}$) so that measurements of the critical fields via magnetic and charge transport methods coincide. However, in a superconducting sample with a type II-to-type I crossover, a superconducting surface state would persist above H_c at temperatures somewhat higher than the crossover at 1.2 K, just as we observe for $H_{c\rho}$. That is, the enhancement of $H_{c\rho}$ in AuBe is associated with the appearance of type II behavior with cooling below T_c in a manner similar to that found for standard superconducting surface states in elemental superconductors with $\kappa \approx 1/\sqrt{2}$. An enhanced $H_{c\rho}$ associated with an impurity phase would show no such connection to the crossover in character of the bulk superconducting phase. In addition, the very small low temperature ρ and relatively large RRR are not consistent with strong scattering at interfaces between crystallites such as would likely occur if an impurity phase was systematically associated with these interfaces. Thus, we are left with the conclusion that the enhancement of $H_{c\rho}$ above H_{c2} is likely to be an intrinsic effect associated with either the surface of our samples, interfaces between crystallites, or twin boundaries between crystallites of opposite structural chirality.

This conclusion is reinforced by the reports of an enhanced $H_{c\rho}$ in several other NCSs including BiPd [60], $LaRhSi_3$ [57,61], $BaPtSi_3$ [62], $LaPdSi_3$ [56], and $LaPtSi_3$ [56] making the observation of this effect a trend in such materials. We have reproduced data from these five NCSs in Fig. 9 for comparison to AuBe. The similarity between $LaRhSi_3$ and AuBe is obvious as both of these materials undergo a transition from type II-to-type I behavior at roughly $0.5T_c$, and both have a region near T_c where H_c and $H_{c\rho}$ coincide [61]. In contrast. BiPd is more robustly type II so that the divergence of H_c and $H_{c\rho}$ occurs much closer to T_c [60]. The similarity of the enhanced critical fields as measured in the resistivity in several NCSs makes problematic sample quality issues less likely as a cause. We point out that it was common to incorrectly dismiss the persistence of superconductivity at high field as due to inhomogeneous samples prior to the discovery of surface superconductivity at fields as large as $1.695H_{c2}$ by Saint-James and de Gennes [18]. However, the cause of the enhanced $H_{c\rho}$ in these NCSs is not clear at this time. In fact, it is expected that even in unconventional cases where there is a spatially modulated order parameter, the surface superconducting state will have the same critical field as predicted in Ref. [18] to first order in $(T_c - T)/T_c$ [55]. This does leave open the possibility that higher-order terms are responsible for an enhancement of H_{c3} far below T_c. Recently, Aoyama *et al.* have suggested that magnetoelectric effects produce an effective magnetic field at twin boundaries of NCSs which can either enhance or reduce the local critical fields [63]. Since both the reduction and enhancement are expected at different symmetry grain boundaries within the same samples, resistivity measurements which are sensitive to filamentary superconducting pathways would display an enhanced critical field in this scenario. However, the small size of the enhancement predicted by these authors is not consistent with the data displayed in Fig. 9.

Because theoretical expectations are not consistent with our data, we are left to speculate about the reason for an enhanced critical field in NCSs as measured by the charge carrier transport far beyond what is expected for a simple surface state in a type II superconductor. Of great recent popularity is the idea that topologically protected superconducting surface states are thought to form on NCS surfaces or interfaces [64]. These interesting states are produced because of symmetry differences at the sample boundaries. Investigations searching for topological surface states in several NCSs including BiPd were not successful. In BiPd, no such states were identified despite the existence of Dirac-type feature in the surface electronic structure 0.7 eV below the Fermi energy [65,66]. The enhanced $H_{c\rho}$ in AuBe, as well as other NCSs displayed in Fig. 9, is immune to the deposition of a magnetic film over its surface, which may be signaling that novel topologically protected states may be present either at surfaces or at twin boundaries of opposing chirality.

Furthermore, we have shown that AuBe displays a nonstandard field dependence of the phase of dHvA oscillations associated with a band thought to host unconventional chiral fermions. This result demonstrates the power of dHvA techniques to establish the properties of a single band despite the presence of other electronic bands with a larger density of states, even in polycrystalline samples. The existence of unusual bulk electronic bands suggests the intriguing possibility of equally unusual, and possibly topological [5], superconducting surface states with enhanced critical fields along with the expectation of Majorana modes. Although we have no direct evidence for these states, nor a demonstrable connection to the novel band evident in the electronic structure calculations and the dHvA oscillations, we point out that

weakly correlated NCSs that have high conductivity such that they display type I or 1.5 behavior may be fruitful places to search for these effects.

ACKNOWLEDGMENTS

J.F.D. acknowledges support through the National Science Foundation (NSF) Grant No. DMR1206763 for the magnetization and charge transport measurements as well as polycrystalline synthesis. P.W.A. acknowledges support through the Department of Energy through Grant No. DE-FG02-07ER46420 for specific-heat measurements, D.P.Y. acknowledges the NSF for support through Grant No. DMR1306392 for single-crystal synthesis, and J.Y.C. the NSF through Grant No. DMR1700030 for structural determination through powder x-ray diffraction. A portion of this work was performed at the National High Magnetic Field Laboratory, which is supported by the NSF Cooperative Agreement No. DMR-1157490 and the state of Florida. J.S. thanks the DoE BES FWP *Science in 100 T* for supporting the development of some of the techniques used in this work. We acknowledge helpful conversations with I. Vekhter and D. Sheehy.

[1] E. Bauer, G. Hilscher, H. Michor, Ch. Paul, E. W. Scheidt, A. Gribanov, Yu. Seropegin, H. Nöel, M. Sigrist, and P. Rogl, Phy. Rev. Lett. **92**, 027003 (2004).

[2] H. Q. Yuan, D. F. Agterberg, N. Hayashi, P. Badica, D. Vandervelde, K. Togano, M. Sigrist, and M. B. Salamon, Phys. Rev. Lett. **97**, 017006 (2006).

[3] A. P. Schnyder, S. Ryu, A. Furusaki, and A. W. W. Ludwig, Phys. Rev. B **78**, 195125 (2008).

[4] R. P. Kaur, D. F. Agterberg, and M. Sigrist, Phys. Rev. Lett. **94**, 137002 (2005).

[5] Guoqing Chang, Benjamin J. Wieder, Frank Schindler, Daniel S. Sanchez, Ilya Belopolski, Shin-Ming Huang, Bahadur Singh, Di Wu, Tay-Rong Chang, Titus Neupert, Su-Yang Xu, Hsin Lin and M. Zahid Hasan, Nat. Mater. **17**, 978 (2018).

[6] Z. Sun, M. Enayat, A. Maldonado, C. Lithgow, E. Yelland, D. C. Peets, A. Yaresko, A. P. Schnyder, and P. Wahl, Nat. Commun. **6**, 6633 (2015).

[7] Mojammel A. Khan, D. E. Graf, I. Vekhter, D. A. Browne, J. F. DiTusa, W. A. Phelan, and D. P. Young, Phys. Rev. B **99**, 020507(R) (2019).

[8] A. B. Karki, Y. M. Xiong, I. Vekhter, D. Browne, P. W. Adams, D. P. Young, K. R. Thomas, J. Y. Chan, H. Kim, and R. Prozorov, Phys. Rev. B **82**, 064512 (2010).

[9] A. Tsvyashchenko, V. Sidorov, A. Petrova, L. Fomicheva, I. Zibrov, and V. Dmitrienko, J. Alloys Compd. **686**, 431 (2016).

[10] S. Mühlbauer, B. Binz, F. Jonietz, C. Pfleiderer, A. Rosch, A. Neubauer, R. Georgii, and P. Boeni, Science **323**, 915 (2009).

[11] B. Matthias, J. Phys. Chem. Solids **10**, 342 (1959).

[12] A. Amon, E. Svanidze, R. Cardoso-Gil, M. N. Wilson, H. Rosner, M. Bobnar, W. Schnelle, J. W. Lynn, R. Gumeniuk, C. Hennig, G. M. Luke, H. Borrmann, and A. Leithe-Jasper, and Yu. Grin, Phys. Rev. B **97**, 014501 (2018).

[13] Drew Rebar, Exploring superconductivity in chiral structured AuBe, Ph.D. dissertation, Louisiana State University, 2015.

[14] B. Bradlyn, J. Cano, Z. Wang, M. G. Vergniory, C. Felser, R. J. Cava, and A. Bernevig, Science **353**, aaf5037 (2016).

[15] P. Tang, Q. Zhou, and S.-C. Zhang, Phys. Rev. Lett. **119**, 206402 (2017).

[16] G. Chang, S.-Y. Xu, B. J. Wieder, D. S. Sanchez, S.-M. Huang, I. Belopolski, T.-R. Chang, S. Zhang, A. Bansil, H. Lin, and M. Z. Hasan, Phys. Rev. Lett. **119**, 206401 (2017).

[17] D. Takane, Z. Wang, S. Souma, K. Nakayama, T. Nakamura, H. Oinuma, Y. Nakata, H. Iwasawa, C. Cacho, T. Kim, K. Horiba, H. Kumigashira, T. Takahashi, Y. Ando, and T. Sato, PRL **122**, 076402 (2019).

[18] D. Saint-James and P. de Gennes, Phys. Lett. **7**, 306 (1963).

[19] Unfortunately, the tiny single crystal was too small to give a reliable signal in the apparatus used for the high-field dHvA experiments [13].

[20] Pei-Chun Ho, J. Singleton, M. B. Maple, Hisatomo Harima, P. A. Goddard, Z. Henkie, and A. Pietraszko, New J. Phys. **9**, 269 (2007).

[21] J. Singleton, J. W. Kim, C. V. Topping, A. Hansen, E.-D. Mun, S. Chikara, I. Lakis, S. Ghannadzadeh, P. Goddard, X. Luo, Y. S. Oh, S.-W. Cheong, and V. S. Zapf, Phys. Rev. B **94**, 224408 (2016).

[22] WIEN2K, an Augmented Plane Wave Plus Local Orbitals Program for Calculating Crystal Properties (2001).

[23] J. P. Perdew, K. Burke, and M. Ernzerhof, Phys. Rev. Lett. **77**, 3865 (1996).

[24] This is a standard benchmark used for density functional theory to test convergence. It is the cutoff in the plane-wave basis, i.e., the muffin tin radius around each atom R multiplied by the plane-wave cutoff value K.

[25] *Inorganic Solid Phases*, edited by Pierre Villars (Springer, Heidelberg, 2016).

[26] B. Cullity, Trans. Am. Instit. Mining Metall. Eng. **171**, 396 (1947).

[27] Hiroaki Okamoto, *Desk Handbook Phase Diagrams for Binary Alloys*, 2nd ed. (ASM International, Materials Park, 2012).

[28] N. N. Greenwood and A. Earnshaw, *Chemistry of the Elements*, 2nd ed. (Butterworth-Heinemann, London, 1997).

[29] Inductive heating is roughly proportional to $(\mathrm{d}H/\mathrm{d}t)^2$ [20]; the fact that data from the upsweeps and downsweeps of the field, where $\mathrm{d}H/\mathrm{d}t$ values are very different (see Fig. 2 of Ref. [21]) overlie suggests that inductive heating is unimportant.

[30] The Landau quantization that is the cause of dHvA oscillations is a result of the magnetic flux density B experienced by the quasiparticles. In a nonmagnetic material such as AuBe, $B = \mu_0 H$, where H is the applied magnetic field, is a very good approximation [31], and so we use B and $\mu_0 H$ reasonably interchangeably.

[31] D. Shoenberg, *Magnetic Oscillations in Metals* (Cambridge University Press, Cambridge, 1984).

[32] P. A. Goddard, J. Singleton, R. D. McDonald, N. Harrison, J. C. Lashley, H. Harima, and M.-T. Suzuki, Phys. Rev. Lett **94**, 116401 (2005)

[33] We Fourier transform the quantity $\mathrm{d}M/\mathrm{d}H = (\mathrm{d}M/\mathrm{d}t)/(\mathrm{d}H/\mathrm{d}t)$. The voltage from the $\dot{B}$ coil $\propto \mathrm{d}H/\mathrm{d}t$ tends to zero as the upper limit of the field sweep is approached. Therefore,

the Fourier windows are truncated 1 or 2 T below the maximum field.

[34] J. F. DiTusa, S. B. Zhang, K. Yamaura, Y. Xiong, J. C. Prestigiacomo, B. W. Fulfer, P. W. Adams, M. I. Brickson, D. A. Browne, C. Capan, Z. Fisk, and J. Y. Chan, Phys. Rev. B **90**, 144404 (2014).

[35] J. Singleton, *Cyclotron Resonance*, in Encyclopedia of Condensed Matter Physics, Vol. 1, edited by F. Bassani, G. L. Liedl and P. Wieder (Elsevier, Oxford, 2005).

[36] M. Hartstein, W. H. Toews, Y.-T. Hsu, B. Zeng, X. Chen, M. Ciomaga Hatnean, Q. R. Zhang, S. Nakamura, A. S. Padgett, G. Rodway-Gant, J. Berk, M. K. Kingston, G. H. Zhang, M. K. Chan, S. Yamashita, T. Saraivara, Y. Takano, J.-H. Park, L. Balicas, N. Harrison *et al.*, Nat. Phys. **14**, 166 (2018).

[37] E. L. Wolf, *A New Paradigm in Condensed Matter and Device Physics* (Oxford University Press, Oxford, 2013).

[38] J.-F. Mercure, A. W. Rost, E. C. T. O'Farrell, S. K. Goh, R. S. Perry, M. L. Sutherland, S. A. Grigera, R. A. Borzi, P. Gegenwart, and A. S. Gibbs, and A. P. Mackenzie, Phys. Rev. B **81**, 235103 (2010).

[39] For example, if the energy shift were such that $F = F_0 + \alpha B$, where α is a constant, the apparent frequency of the oscillations would remain constant, but their phase would shift [see Eq. (7)] [40].

[40] J. Singleton, R. J. Nicholas, F. Nasir, and C. K. Sarkar, J. Phys. C: Solid State Phys. **19**, 35 (1986).

[41] S. E. Sebastian, N. Harrison, C. D. Batista, S. A. Trugman, V. Fanelli, M. Jaime, T. P. Murphy, E. C. Palm, H. Harima, and T. Ebihara, Proc. Natl. Acad. Sci. USA **106**, 7741 (2009).

[42] N. W. Ashcroft and N. D. Mermin, *Solid State Physics* (Holt, Reinhart and Winston, New York, 1976).

[43] We note that the authors of Ref. [12] obtain $\theta_D = 388$ K. There is an error in their equivalent of our Eq. (10). However, this does not seem to be enough to account for the difference in values of θ_D. After numerous careful checks with data from two measurements, we believe that our value of θ_D is correct.

[44] B. Mühlschlegel, Z. Phys. **155**, 313 (1959).

[45] M. Tinkham, *Introduction to Superconductivity*, 2nd ed., Dover Books on Physics, Vol. 1 (Dover, New York, 2004).

[46] A. Aharoni, J. Appl. Phys. **83**, 3432 (1998).

[47] H. Leng, C. Paulsen, Y. K. Huang, and A. de Visser, Phys. Rev. B **96**, 220506(R) (2017).

[48] R. A. Hein and R. L. Falge, Phys. Rev. **123**, 407 (1961).

[49] L. L. Zhao, S. Lausberg, H. Kim, M. A. Tanatar, M. Brando, R. Prozorov, and E. Morosan, Phys. Rev. B **85**, 214526 (2012).

[50] James Annett, *Superconductivity, Superfluids and Condensates* (Oxford University Press, Oxford, 2004).

[51] U. Krägeloh, Phys. Lett. A **28**, 657 (1969).

[52] J. Auer and H. Ullmaier, Phys. Rev. B **7**, 136 (1973).

[53] E. Babaev, J. Carlström, M. Silaev, and J. M. Speight, Phys. C (Amsterdam) **533**, 20 (2017); *Superfluid States of Matter*, 1st ed., edited by Boris V. Svistunov, Egor S. Babaev, and Nikolay V. Prokof'ev (CRC Press, Boca Raton, FL, 2015).

[54] V. P. Mineev and K. V. Samokhin *Introduction to Unconventional Superconductivity* (Gordon and Breach, Amsterdam, 1999).

[55] See, e.g., *Non-centrosymmetric Superconductors, Introduction and Overview*, edited by E. Bauer and M. Sigrist (Springer, Berlin, 2012), and references therein.

[56] M. Smidman, A. D. Hillier, D. T. Adroja, M. R. Lees, V. R. Anand, R. P. Singh, R. I. Smith, D. M. Paul, and G. Balakrishnan, Phys. Rev. B **89**, 094509 (2014).

[57] N. Kimura, N. Kabeya, K. Saitoh, K. Satoh, H. Ogi, K. Ohsaki, and H. Aoki, J. Phys. Soc. Jpn. **85**, 024715 (2016).

[58] V. K. Anand, D. Britz, A. Bhattacharyya, D. T. Adroja, A. D. Hillier, A. M. Strydom, W. Kockelmann, B. D. Rainford, and K. A. McEwen, Phys. Rev. B **90**, 014513 (2014).

[59] K. Wakui, S. Akutagawa, N. Kase, K. Kawashima, T. Muranaka, Y. Iwahori, J. Abe, and J. Akimitsu, J. Phys. Soc. Jpn. **78**, 034710 (2009).

[60] M. Khan, Ph.D. thesis, Louisiana State University, 2017.

[61] N. Kimura, H. Ogi, K. Satoh, G. Ohsaki, K. Saitoh, H. Iida, and H. Aoki, JPS Conf. Proc. **3**, 015011 (2014).

[62] E. Bauer, R. Khan, H. Michor, E. Royanian, A. Grytsiv, N. Melnychenko-Koblyuk, P. Rogl, D. Reith, R. Podloucky, E.-W. Scheidt *et al.*, Phys. Rev. B **80**, 064504 (2009).

[63] K. Aoyama, L. Savary, and M. Sigrist, Phys. Rev. B **89**, 174518 (2014).

[64] A. P. Schnyder, P. Brydon, and C. Timm, Phys. Rev. B **85**, 024522 (2012).

[65] M. Neupane, N. Alidoust, M. M. Hosen, J.-X. Zhu, K. Dimitri, S.-Y. Xu, N. Dhakal, R. Sankar, I. Belopolski, D. S. Sanchez *et al.*, Nat. Commun. **7**, 13315 (2016).

[66] S. Thirupathaiah, S. Ghosh, R. Jha, E. Rienks, K. Dolui, V. R. Kishore, B. Büchner, T. Das, V. Awana, D. Sarma *et al.*, Phys. Rev. Lett. **117**, 177001 (2016).